

# Atmospheric rivers and water fluxes in precipitating quasi-geostrophic turbulence

Thomas K. Edwards<sup>1</sup>  | Leslie M. Smith<sup>1,2</sup> | Samuel N. Stechmann<sup>1,3</sup>

<sup>1</sup>Department of Mathematics, University of Wisconsin-Madison, Madison, Wisconsin, USA

<sup>2</sup>Department of Engineering Physics, University of Wisconsin-Madison, Madison, Wisconsin, USA

<sup>3</sup>Department of Atmospheric and Oceanic Sciences, University of Wisconsin-Madison, Madison, Wisconsin, USA

## Correspondence

T. K. Edwards, Department of Mathematics, 480 Lincoln Drive, Madison, WI 53706, USA  
Email: [tkedwards@wisc.edu](mailto:tkedwards@wisc.edu)

## Funding information

National Science Foundation Division of Atmospheric and Geospace Sciences the NSF Division of Mathematical Sciences the Wisconsin Alumni Research Foundation, Grant/Award Numbers: 1443325, 1147523

## Abstract

Most of the poleward transport of water can be accounted for by long narrow corridors known as Atmospheric Rivers (ARs). ARs are typically associated with extratropical cyclones and, for dry extratropical cyclones, an idealized prototype has previously been provided by quasi-geostrophic (QG) dynamics. However, there are few if any studies that investigate ARs in a QG framework. Here, the overarching question is: do idealized ARs appear in moist QG dynamics? A precipitating quasi-geostrophic (PQG) model is explored as a possible prototype for ARs and associated water transport. The set-up uses numerical simulations of geostrophic turbulence with precipitation, in a single phase. The simulations are shown to produce idealized ARs, and they have reasonably realistic statistics for such a simple set-up. For instance, the model ARs occur roughly as frequently as in nature, based on commonly used AR identification algorithms. To produce ARs in this model, it is found that two key ingredients are needed beyond the dry QG framework: precipitation and a meridional moisture gradient. If either of these two ingredients is too weak, then less realistic ARs are produced. In addition, for a range of precipitation rates, a large fraction of the meridional moisture transport is due to ARs.

## KEY WORDS

atmospheric rivers, meridional moisture transport, precipitating quasi-geostrophic, two-level QG, water flux

## 1 | INTRODUCTION

Atmospheric Rivers (ARs) are an important source of water transport in the atmosphere. They can carry more water than 7–15 Mississippi Rivers combined (Ralph and Dettinger, 2011) and are reported to be able to transport more than 90% of the total midlatitude vertically integrated water vapour flux (Zhu and Newell, 1998; Gimeno *et al.*, 2014). Due to the amount of water within these ARs, when one passes over a coastal area with mountainous

topography it can provide significant amounts of precipitation. For example, a study by Smith *et al.* (2010) saw that about 20–40% of the water vapour in a particular atmospheric river rained out over northern California in a storm on 29–31 December 2005. Moreover, in this region and other coastal locations, a significant portion of the annual precipitation is found to be due to AR contributions (Dettinger, 2011; Ralph *et al.*, 2013; Rutz *et al.*, 2014).

An AR is defined in the Glossary of Meteorology to be “a long, narrow, and transient corridor of strong horizontal

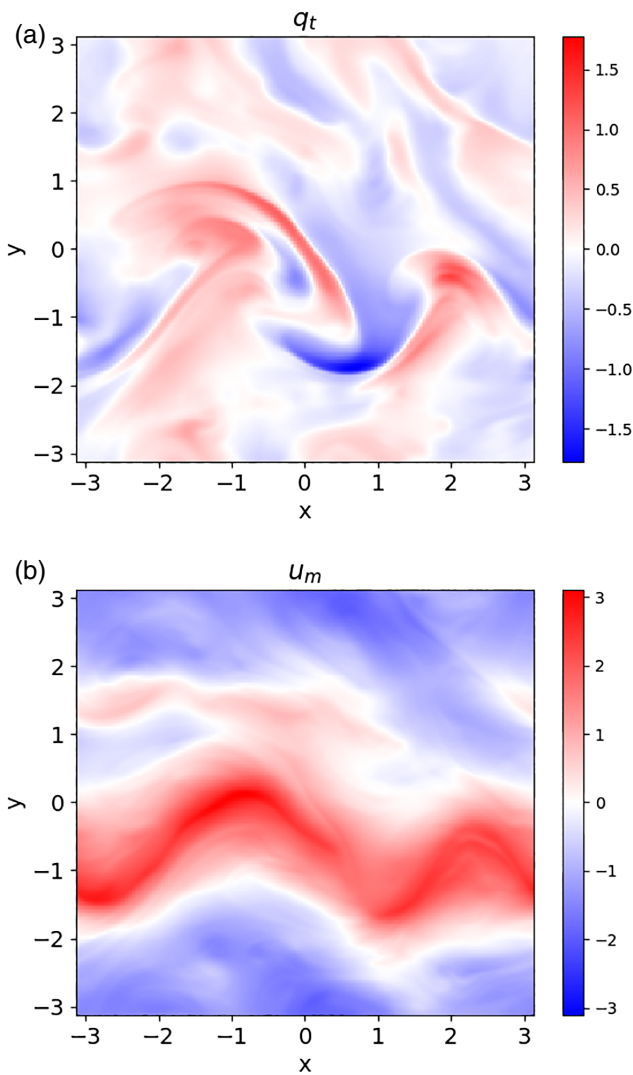


**FIGURE 1** Example 1: A snapshot at  $t = 700$  of (a) total water,  $q_t$ , and (b) corresponding horizontal velocity at the mid-level,  $u_m$ , where the total water is long, narrow and filamented, suggestive of ARs.  $V_r = 1$  and  $Q_y = -1$ . The domain ( $x, y$ ) is doubly periodic [Colour figure can be viewed at [wileyonlinelibrary.com](http://wileyonlinelibrary.com)]

water vapor transport that is typically associated with a low-level jet stream ahead of the cold front of an extratropical cyclone" (Ralph *et al.*, 2018), Dacre *et al.* (2015) and Gimeno *et al.* (2016) provide more discussion on the causes of ARs.

Motivation for this study is provided by the long and filamented regions of water found in snapshots of our precipitating quasi-geostrophic (PQG) simulations, such as those in Figure 1, which resembled ARs. Studies of ARs have mostly been done using observational data or data from complex models. Here we ask: do atmospheric rivers form in a simple model, and if so, what is their collective contribution to meridional transport in the model?

To investigate these questions, a quasi-geostrophic (QG) framework is used as it is simple enough to

understand theoretically, yet complex enough to have interesting behaviour. Past achievements based on the quasi-geostrophic equations include theoretical and numerical analyses of the baroclinic instability (Charney, 1947; 1948; Phillips, 1954) and geostrophic turbulence (Rhines, 1979; Salmon, 1980). These results have helped to describe the dynamics in the extratropics.

Observational studies of ARs suggest that it might be possible to produce idealized ARs within a QG framework. In particular, ARs are typically associated with extratropical cyclones, and the quasi-geostrophic equations are often used as a prototype model for cyclones, baroclinic eddies, and zonal jets. Furthermore, some studies have used QG thinking in their analysis of observed ARs (Cordeira *et al.*, 2013; Hecht and Cordeira, 2017), and it has been proposed that the uplift of moisture in regions of horizontal convergence leads to some properties of the ARs (Dacre *et al.*, 2015). Hence many AR processes are in principle present within the QG framework.

While the ARs in the QG framework may be less sharp than in nature if the model lacks fronts, it is hoped that this simple framework can nevertheless serve as a foundation from which to build mechanistic understanding. For instance, within a QG framework, one can investigate what an AR might look like in the absence of frontogenesis and frontogenetic uplift. If certain aspects are lacking from the QG ARs, they serve as candidate aspects that are associated with frontogenesis in particular, beyond QG aspects of baroclinic eddies.

There are several variations/adaptations of the dry QG equations to include water substance (e.g., Mak, 1982; Bannon, 1986; Lapeyre and Held, 2004; Lambaerts *et al.*, 2012; Monteiro and Sukhatme, 2016; Smith and Stechmann, 2017), which have provided insight into moist dynamics and the role of latent heat release in the atmosphere. Here we will use the PQG equations derived in Smith and Stechmann (2017). A notable property of the PQG equations is that they are asymptotic limiting equations of a cloud-resolving model, and thus they allow for phase changes of water, latent heat release and precipitation (e.g., Kessler, 1969; Hernandez-Duenas *et al.*, 2013).

Using the PQG model in a saturated environment, we show the presence of ARs, as well as the fact that some of these ARs can represent a large percentage of the meridional flux. We also investigate how the meridional gradient of water and rainfall impact water transport within the model. Moisture transport in a saturated environment was previously investigated using the linearized PQG model (Wetzel *et al.*, 2017), whereas here we study nonlinear dynamics. It would be interesting in the future to investigate the dynamics with phase changes, in which case further realism can be included. Here, in the saturated

case without phase changes, a linear eigenmode perspective can be taken (as in Edwards *et al.*, 2019), and precipitation effects can be included in a simple way with the fewest number of parameters and without additional complexities.

The paper is organized as follows. In Section 2, we present the two-level, single-phase (saturated – i.e., no phase changes) PQG equations on a  $\beta$ -plane. Section 3 describes the numerical method used in our simulations, as well as the algorithm used to identify PQG atmospheric rivers. In Section 4, there is a discussion of the characteristics of the model atmospheric rivers. In Section 5, we examine the effects of rainfall and background moisture gradient on the meridional transport of water. In Section 6, we describe additional parameter studies. The discussion and conclusion are given in Section 7.

## 2 | DESCRIPTION OF PRECIPITATING QG EQUATIONS

The PQG equations (Smith and Stechmann, 2017) are a moist version of the QG equations. Here we present a brief overview of the PQG equations, in a two-level set-up. Salmon (1998), Vallis (2006) and Pedlosky (2013) give background and derivations of the *dry* QG equations.

Considering the most basic version of PQG, we do not allow for phase changes. In a saturated environment, the anomalous contribution to the total water,  $q_t$ , is equal to the anomalous rain water,  $q_r$ :

$$q_t = q_r. \quad (1)$$

Using Equation (1), the non-dimensional version of saturated, two-level PQG on a  $\beta$ -plane may be written as:

$$\frac{D_1 PV_1}{Dt} + \beta v_1 = 0, \quad (2a)$$

$$\frac{D_2 PV_2}{Dt} + \beta v_2 = 0, \quad (2b)$$

$$\frac{D_m M}{Dt} = -\frac{V_r}{\Delta z} q_r = -\frac{V_r}{\Delta z} (M - G_M \theta_e), \quad (2c)$$

with

$$PV_1 = \nabla_h^2 \psi_1 + \left( \frac{1}{\Delta z} \frac{L}{L_{ds}} \right)^2 (\psi_2 - \psi_1), \quad (3a)$$

$$PV_2 = \nabla_h^2 \psi_2 + \left( \frac{1}{\Delta z} \frac{L}{L_{ds}} \right)^2 (\psi_1 - \psi_2), \quad (3b)$$

$$\theta_e = \frac{L}{L_{ds}} \frac{\psi_2 - \psi_1}{\Delta z}, \quad (3c)$$

$$u_i = -\frac{\partial \psi_i}{\partial y} \quad \text{for } i = 1, 2, \quad (3d)$$

$$v_i = \frac{\partial \psi_i}{\partial x} \quad \text{for } i = 1, 2, \quad (3e)$$

$$u_m = \frac{u_1 + u_2}{2}, \quad (3f)$$

$$v_m = \frac{v_1 + v_2}{2}. \quad (3g)$$

Here,  $u_j, v_j$  represent the horizontal components of the fluid velocity at level  $j$ , for the two levels  $j = 1, 2$ , or  $j = m$  for the mid-level (the level in the middle of the domain; between level 1 and level 2);  $\theta_e$  represents the equivalent potential temperature, and  $q_t, q_r$  represent the total water and rain water, respectively. Note that all variables are functions of two spatial variables  $(x, y)$  and time,  $t$ . We use the notation

$$\frac{D_1}{Dt}(\cdot) = \partial_t(\cdot) + u_1 \partial_x(\cdot) + v_1 \partial_y(\cdot),$$

and similarly for  $D_2(\cdot)/Dt$  and  $D_m(\cdot)/Dt$ . In the QG, the (depth-)averaged velocities  $u_m$  and  $v_m$  are commonly known as the barotropic velocities. Note that the thermodynamic variables  $\theta_e, M, q_t$  are all located at the mid-level (the level in the middle of the domain; between level 1 and level 2), and subscript  $m$  will be left out to reduce notation. Summaries of the variables, parameters, and symbols are provided in Tables 1–4.

Notice that the PQG equations use two prognostic variables: the potential vorticity (as in dry QG) as well as a second variable  $M$  which is not part of dry QG. The evolution of  $M$  is described in Equation (2), and  $M$  is defined as

$$M = q_t - G_M \theta_e, \quad (4)$$

where the parameter  $G_M$  is defined in Table 3. With the inclusion of water, an additional dynamical equation is needed, in addition to the *PV* equations. While one could use the equation for  $q_t$  as the additional equation, the  $q_t$  equation has the disadvantage of containing a term involving the vertical velocity  $w$ :

$$\frac{D_m q_t}{Dt} - G_M \frac{L_{ds}}{L} w = -\frac{V_r}{\Delta z} q_t, \quad (5a)$$

$$\frac{D_m \theta_e}{Dt} + \frac{L_{ds}}{L} w = 0. \quad (5b)$$

Hence, it is more convenient and consistent to use a dynamical moisture equation which also does not explicitly require  $w$ . To obtain such an equation, we define  $M$  to be a special linear combination of  $q_t$  and  $\theta_e$ , chosen to eliminate  $w$  by combining Equations (5a) and (5b), which leads to the choice of  $M = q_t - G_M \theta_e$ . A similar idea is used in dry QG: the dynamical equation for vorticity includes the influence of  $w$ , but a *PV* variable can be formed which eliminates the influence of  $w$ . The

Symbol	Definition
$\mathbf{x} = (x, y, z)$	Horizontal coordinates
$t$	Time
$\mathbf{u}(\mathbf{x}, t) = (u, v, w)$	Velocities
$\mathbf{u}_h = (u, v)$	Horizontal velocities
$\zeta(\mathbf{x}, t) = \partial_x v - \partial_y u$	Relative vorticity
$\psi(\mathbf{x}, t)$	Streamfunction (pressure scaled by constant density)
$\theta$	Potential temperature
$q_v(\mathbf{x}, t)$	Water vapour mixing ratio
$q_r(\mathbf{x}, t)$	Rain water mixing ratio
$q_t(\mathbf{x}, t) = q_v + q_r$	Total water mixing ratio
$\theta_e(\mathbf{x}, t) = \theta + q_v$	Equivalent potential temperature
$PV(\mathbf{x}, t) = \nabla_h^2 \psi + (L/L_{ds})^2 (\partial^2 \psi / \partial z^2)$	Potential vorticity
$M(\mathbf{x}, t) = q_t + G_M \theta_e$	Thermodynamic variable $M$

**TABLE 1** Definition of variables

**TABLE 2** Dimensional parameters and typical values

Symbol	Unit	Definition
$L$	1,000 km	Horizontal reference length scale for QG
$L_{ds}$	700 km	Saturated Rossby deformation radius
$c_p$	$10^3 \text{ J} \cdot \text{kg}^{-1} \cdot \text{K}^{-1}$	Specific heat
$L_v$	$2.5 \times 10^6 \text{ J}$	Latent heat factor
$d\tilde{\theta}_e/dz$	$1.5 \text{ K} \cdot \text{km}^{-1}$	Background vertical gradient of equivalent potential temperature
$d\tilde{q}_t/dz$	$-0.6 \text{ g} \cdot \text{kg}^{-1} \cdot \text{km}^{-1}$	Background vertical gradient of total water
$V_T$	$0.3 - 10 \text{ m} \cdot \text{s}^{-1}$	Rainfall speed (Precipitation intensity)
$U_0$	$10 \text{ m} \cdot \text{s}^{-1}$	Characteristic midlatitude horizontal velocity
$W_0$	$0.1 \text{ m} \cdot \text{s}^{-1}$	Characteristic vertical velocity
$\beta_0$	$2.5 \times 10^{-11} \text{ m}^{-1} \cdot \text{s}^{-1}$	Change in rate of rotation

**TABLE 3** Non-dimensional parameters

Parameter	Definition
$L/L_{ds}$	Non-dimensional ratio of length scales
$\beta = L^2 \beta_0 / U_0$	Non-dimensional change in rate of rotation
$G_M = -L_v c_p^{-1} (d\tilde{q}_t/dz) (d\tilde{\theta}_e/dz)^{-1}$	Ratio of the background vertical gradients of $q_r$ and $\theta_e$
$V_r = V_T / W_0$	Non-dimensional rainfall speed

**TABLE 4** Notation for symbols

Notation	Definition
$D/Dt = \partial_t + \mathbf{u} \cdot \nabla_h$	Material derivative
$\nabla_h = \hat{\mathbf{x}} \partial_x + \hat{\mathbf{y}} \partial_y$	Horizontal Laplacian
$D_h/Dt = \partial_t + \mathbf{u}_h \cdot \nabla_h$	Horizontal material derivative
$(\cdot)_1$	$(\cdot)$ at level 1
$(\cdot)_2$	$(\cdot)$ at level 2
$(\cdot)_m$	$(\cdot)$ at the mid-domain (between levels 1 and 2)

combined result, for PQG, is the system in Equation (2), where  $w$  has been eliminated from all prognostic evolution equations.

Note that latent heating is included, even in this saturated set-up without phase changes. The latent heating term can be seen, for example, in the budget of potential temperature in equation (23) of Smith and Stechmann (2017). The latent heating is implicitly included in the model, even though it does not appear explicitly in the equations above, which were formulated in terms of the thermodynamic variables  $q_t$  and  $\theta_e$  in Equations (5a) and (5b). At the same time, latent heating (positive  $w$ ) and latent cooling (negative  $w$ ) are both present, and an asymmetry in vertical velocity is not promoted. A case with phase changes would be interesting in part because of its potential for up-down asymmetry, among other reasons, and is an interesting future case to consider. Here, in a saturated set-up, the effects of a precipitation term can be studied in a simpler setting.

There are four non-dimensional parameters in Equation (2) (Table 3), two from the dry physics and two from the moist physics. Readers familiar with QG will recognize the length-scale ratio,  $L_{ds}/L$ , and the change in the rotation rate with latitude,  $\beta$  (e.g., Salmon, 1998; Vallis, 2006; Pedlosky, 2013). The length-scale  $L$  is a horizontal reference length-scale. The (saturated) Rossby deformation radius  $L_{ds}$  is defined in terms of more fundamental quantities as  $L_{ds} = N_s H/f$ , where  $f$  is the rotation rate,  $H$  is the reference height, and  $N_s$  is the (saturated) buoyancy frequency or Brunt–Vaisala frequency. Its square  $N_s^2$  is defined as  $N_s = (g/\theta_0) d\theta_e/dz$ , where  $g$  is the gravitational acceleration, and  $\theta_0$  is a typical surface value of temperature. In essence,  $L_{ds} = N_s H/f$  is the length-scale at which rotation becomes as important as buoyancy for a saturated region.

In addition to those two dry parameters, there are the two parameters associated with moisture: the ratio of the background vertical gradients of total water and equivalent potential temperature,  $G_M$ , and the rainfall speed,  $V_r$ . Note that  $V_r$  in the model is best interpreted as a proxy for the amount of rainfall, rather than as a speed associated with droplets.

Similar to the dry case, the two-level Equations (2) were obtained by taking a finite difference in  $z$  of the continuously stratified PQG equations. As is commonly done in the dry case, the boundary condition  $\theta_e = 0$  is imposed at both the top and bottom boundaries (e.g., as in Held and O'Brien, 1992). For the moist equations, we apply the additional constraint of zero water inflow at the top boundary. In the horizontal directions, doubly periodic boundary conditions are imposed. Edwards *et al.* (2019) provide more details regarding the derivation of the equations and the boundary conditions.

### 3 | METHODS AND ALGORITHMS

#### 3.1 | Simulation details

To investigate the structure and statistics of ARs and water transport, Equations (2) are initialized with baroclinically unstable conditions (Salmon, 1998; Vallis, 2006; Pedlosky, 2013). Furthermore, the instability will help to drive the system to a statistical steady state, and the instability arises from imposing a background zonal flow with constant vertical shear  $U$ , and a background equivalent potential temperature, decreasing from south to north with constant gradient  $\Theta$ . Then the equations take the form:

$$\begin{aligned} \frac{D_1 PV_1}{Dt} - U \partial_x PV_1 + v_1 \partial_y PV_{1,bg} + \beta v_1 \\ = -\kappa_M \Delta \psi_1 - v \Delta^4 PV_1, \end{aligned} \quad (6a)$$

$$\begin{aligned} \frac{D_2 PV_2}{Dt} + U \partial_x PV_2 + v_2 \partial_y PV_{2,bg} + \beta v_2 \\ = -v \Delta^4 PV_2 \end{aligned} \quad (6b)$$

$$\begin{aligned} \frac{D_m M}{Dt} + v_m \partial_y M_{bg} \\ = -\frac{V_r}{\Delta z} (M - G_M \theta_e) - v \Delta^4 M, \end{aligned} \quad (6c)$$

where the background meridional gradients of potential vorticity are labelled as  $PV_{1,bg}$  and  $PV_{2,bg}$ .

For consistency within the QG framework, the values of  $U$ ,  $\Theta$ ,  $PV_{1,bg}$  and  $PV_{2,bg}$  are all related by one free parameter, for example,  $\Theta$ ,  $PV_{1,bg}$  and  $PV_{2,bg}$  may be determined from the value of  $U$  (Salmon, 1998; Vallis, 2006; Pedlosky, 2013). A constant background meridional gradient of water,  $Q_y$ , is also included such that the background  $M$  term is given by  $M_{bg} = (Q_y + G_M \Theta) y$ . Additional dissipation terms of fourth-order hyperviscosity and lower-level friction were also included (also Edwards *et al.*, 2019).

Equations (6) were evolved using a pseudospectral solver on a doubly periodic domain in the horizontal directions, with three-halves padding for de-aliasing. Time-stepping was done by a third-order Runge–Kutta scheme with an adaptive  $\Delta t$  chosen to satisfy the Courant–Friedrichs–Lowy (CFL) condition to ensure that the numerical time integration is stable. In brief, this means that the time step  $\Delta t$  is chosen to be smaller than each of the reference time-scales of the system, such as the advective time-scale  $\Delta x/u$ , the baroclinic wave time-scale, and the hyperviscosity time-scale. Since the advective time-scale is defined in terms of the velocities  $u(x, y, t)$  and  $v(x, y, t)$  which are evolving in time, the time step  $\Delta t$  will be adaptive in the sense that a different  $\Delta t$  value could arise at different times, depending on the velocity values. Most of the simulations used resolution  $N^2 = 256^2$  Fourier modes for approximately 400 days, in order to allow for a large

number of over 70 simulations across different parameter values. Additional simulations with higher resolution of  $N^2 = 512^2$  showed ARs that look essentially the same, since the precipitation creates ARs that are synoptic-scale features and are somewhat coherent. The initial condition was a band of eigenmodes centred around the unstable wave-vector  $(k, l) = (3, 1)$ , and the simulations were run long enough to obtain statistical steady states. More details about the eigenmodes can be found in the appendix of Edwards *et al.* (2019).

The dry parameter values are  $\beta = 2.5$ ,  $\kappa_M = 0.05$ ,  $v = 5 \times 10^{-15}$  and  $k_{ds} = 4$ , and were chosen to match the (dry) midlatitude atmosphere case studied in Qi and Majda (2016). Instead of the value  $U = 0.2$  as in their study, we used the value  $U = 0.25$  because it produced a jet with more undulations, and was thus more conducive to the formation of ARs.

The parameters reflecting the presence of water are  $G_M$ ,  $Q_y$  and  $V_r$ . Recall that  $G_M$  depends on the background vertical gradient of water, and  $Q_y$  is the background meridional gradient of water. Unless otherwise noted, we fix the values  $G_M = 1$  and  $Q_y = -1$  such that

$$M_{bg} = (Q_y + G_M \Theta)y = (-1 + \Theta)y.$$

As mentioned above, the parameter  $V_r$  can be interpreted as a surrogate for the total amount of precipitation, and we study the characteristics of PQG atmospheric rivers with varying  $V_r$ .

### 3.2 | Atmospheric river identification algorithm

There are several methods to identify ARs, most of which depend on intensity and/or geometry thresholds. These can be largely split into three categories (Guan and Waliser, 2015):

(a) methods which use a single observation site or model grid cell (e.g., Neiman *et al.*, 2009; Dettinger, 2011; Ralph *et al.*, 2013);

(b) methods which track pre-selected cross-sections while satisfying a set criteria for the geometry and intensity (e.g., Lavers *et al.*, 2011; Lavers *et al.*, 2012; Nayak *et al.*, 2014; Gao *et al.*, 2015); and

(c) methods which consider geometry and intensity thresholds throughout the domain and identifying any ARs in the domain (e.g., Wick *et al.*, 2013; Jiang *et al.*, 2014; Rutz *et al.*, 2014; Guan and Waliser, 2015).

The first method is useful for studying AR landfalls in small, local areas; the second method is applied in regional

studies concerning AR landfalls; and the third method is for larger domains, where the interest is not only on AR landfalls.

In addition, the algorithms typically depend on either integrated water vapour (IWV), or integrated vapour transport (IVT). In earlier works, IWV was used to identify and measure the AR's intensity and spatial distribution (e.g., in Ralph *et al.*, 2004; Neiman *et al.*, 2008) since these studies used satellite-based observations. However, more recently, IVT has been used because it is more directly related to precipitation and depends less on surface elevation (e.g., in Rutz *et al.*, 2014; Ralph *et al.*, 2019).

Here, the method to identify ARs is essentially based on the algorithm found in Guan and Waliser (2015), which is a method in the third family. A choice from the third family was used because our model has no topography and therefore does not investigate AR landfalls, and also because of the fact that it can be used to study large scales, and does not require a pre-selection of a cross-section. To be consistent with their algorithm, we also chose IVT to be the variable of interest over IWV. As our model only has  $q_t(z)$  at  $z = z_m$  (at the mid-level), the  $q_t$  will be assumed to be independent of  $z$  for simplicity.

The general idea is to identify locations of high intensity with the correct orientation, and that also have specific geometries (long and thin). First, to find high-intensity IVT regions, the algorithm identifies connected regions in which the magnitude of the water transport is at least at the 85th percentile. The direction of mean water transport is then determined for each of these regions, and compared to the water transport direction in each cell. If the direction of water transport in more than half of the grid cells deviates by more than  $45^\circ$  from the direction of mean water transport, then the region is removed from the possible candidates for an AR.

To determine if the high-intensity IVT regions have the correct geometry, the line connecting the two points which are furthest apart from each other, known as the major axis, is first identified. If the orientation of the major axis differs from the direction of the mean water transport direction by more than  $45^\circ$ , this region is also discarded.

For each remaining candidate AR, the length is considered to be the length of the major axis. The width is computed by taking the area of each such candidate region and dividing by the length. If the region has a length greater than a length threshold, and if it also has a ratio of length/width greater than 2, then we define this to be an AR. In Guan and Waliser (2015), a length threshold of 2,000 km is used, whereas in our case, because the domain is smaller, we use an adjusted threshold of 1,000 km.

## 4 | CHARACTERISTICS OF QG ATMOSPHERIC RIVERS

In this section we explore to what extent atmospheric rivers appear, the characteristics that they have, and also the effect of varying the rainfall parameter  $V_r$  on the number of occurrences of the ARs.

As background for comparison with the model, in nature most ARs appear as very long and thin corridors of water transport, a typical example being a long filament reaching from the Hawaiian islands to northern California. Moreover, ARs are known to carry a large percentage of meridional water flux (Zhu and Newell, 1998). There is a tendency for ARs to appear more frequently in the winter, due to the strong association with extratropical cyclones (Gimeno *et al.*, 2014). For the time period 2008–2010, Waliser *et al.* (2012) counted a total of 259 ARs (122 for the first year; 137 for the second), in roughly five different regions (Northeast Pacific, Southeast Pacific, North Atlantic, South Atlantic, South Indian) with approximately a quarter of the ARs making landfall.

We present two examples of ARs identified by the algorithm mentioned in Section 3.2. Figures 1 and 2 show the anomalous total water,  $q_t$ , and the zonal velocity,  $u_m$ . Both figures show that  $q_t$  is concentrated in filamentary regions located within the eastward zonal jet. Away from the eastward zonal jet, the  $q_t$  anomalies are weaker and less filamentary.

Figures 3 and 4 show the ARs that were identified and the accompanying snapshots of  $uq_t$  and  $vq_t$  fields used as part of the AR identification algorithm. The regions of strongest water transport in the  $x$  and  $y$  direction are, as one would expect, regions where  $q_t$  and  $u, v$  are strong. These regions appear to correspond with the locations of the strongest winds of the zonal jet in the cases represented by Figures 3 and 4. The AR in Figure 4 especially shows that these structures can appear to be long and filamentary, like those seen in nature (e.g., Neiman *et al.*, 2008; Ralph *et al.*, 2019, for ARs in nature).

Interestingly, in Figures 1 and 3, while the filamentary region in  $1 \leq x \leq 3, -2 \leq y \leq 0$  looks like an AR by eye, it is not captured by the algorithm. As mentioned above, the following factors could cause this region to be excluded as an AR: the total magnitude of the water flux does not meet the threshold value; the region does not have the required geometry; or the geometry does not match the water transport direction.

Since the PQG model has a proxy parameter for the amount of precipitation,  $V_r$ , one might ask how the rainfall parameter  $V_r$  affects the occurrences of ARs. Thus we compared simulations with seven values of  $V_r$  in the range  $0.01 \leq V_r \leq 10$ , with all other parameters held fixed.

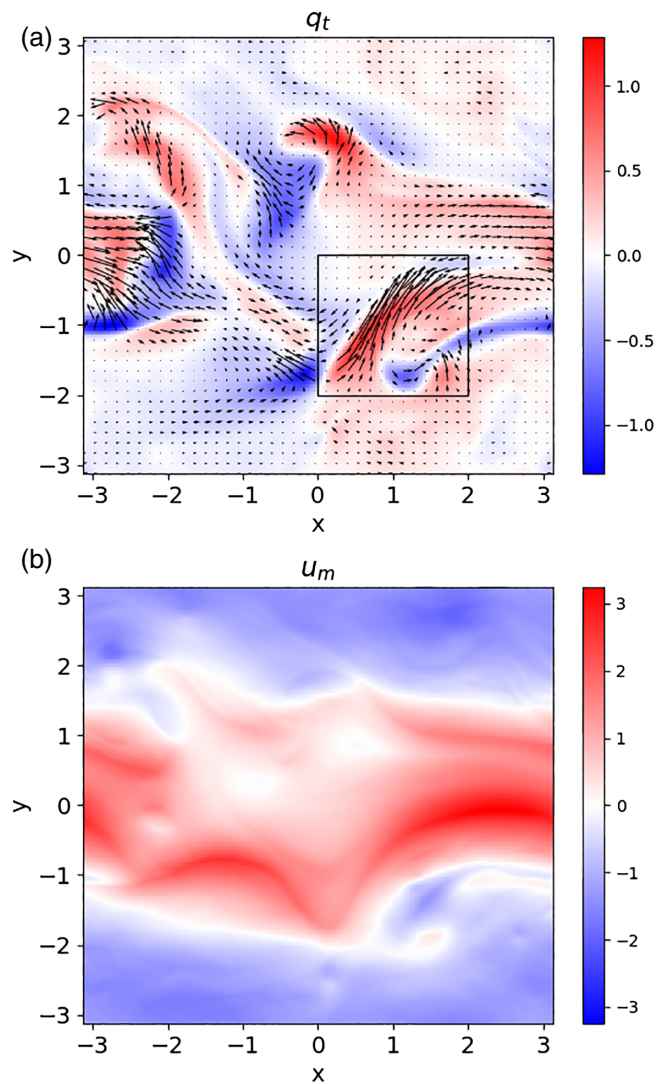


**FIGURE 2** Example 2. Snapshot at  $t = 360$  of (a)  $q_t$  and (b)  $u_m$ , with  $V_r = 1$  and  $Q_y = -1$ . The arrows in (a) represent the intensity and direction of the water transport ( $uq_t, vq_t$ ) [Colour figure can be viewed at [wileyonlinelibrary.com](http://wileyonlinelibrary.com)]

For each value of  $V_r$ , we ran 10 simulations using different initial conditions for  $q_t$ , and counted the number of ARs detected by the algorithm in each simulation. To ensure that we did not count the same ARs more than once, we ran the algorithm on snapshots taken 20 time units apart (one time unit corresponds to approximately one day). In Figure 5, the vertical lines show the span of AR counts for the ten different simulations, and each circle indicates the average number of ARs for the simulation group with fixed  $V_r$ .

As seen from Figure 5, for  $V_r$  values which are  $\mathcal{O}(1)$  or less, the number of occurrences of ARs are  $\mathcal{O}(10)$  and for  $V_r$  that are larger, there are approximately an order of magnitude less. As a possible explanation, in this model, it is known that for large  $V_r$  ( $> \mathcal{O}(10)$ ),  $q_t$  will largely resemble the vertical velocity,  $w$ , and will show less influence from

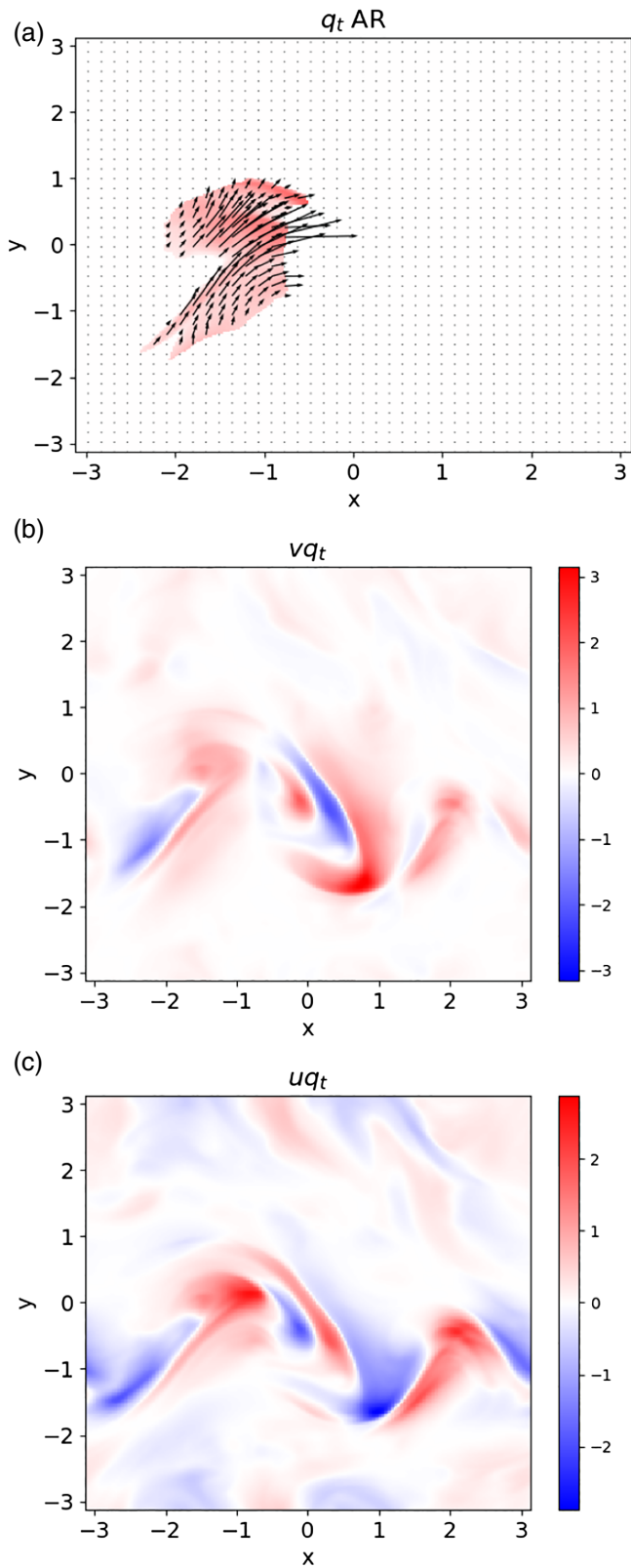


**FIGURE 3** Example 1. Snapshot at  $t = 700$  of (a) river, (b)  $vq_t$ , and (c)  $uq_t$ , with  $V_r = 1$  and  $Q_y = -1$ . The arrows in (a) represent the intensity and direction of the water transport ( $uq_t, vq_t$ ) [Colour figure can be viewed at [wileyonlinelibrary.com](http://wileyonlinelibrary.com)]

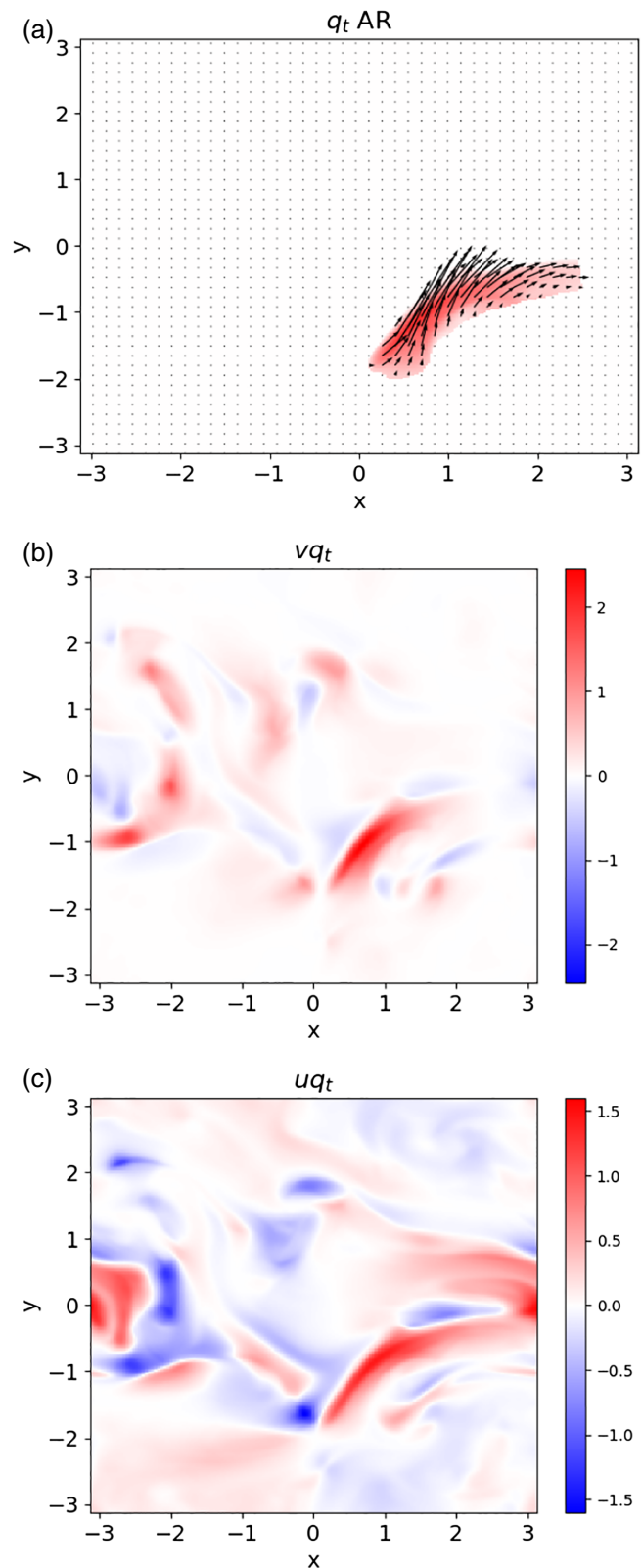


**FIGURE 4** Example 2. As Figure 3, but at  $t = 360$ . [Colour figure can be viewed at [wileyonlinelibrary.com](http://wileyonlinelibrary.com)]

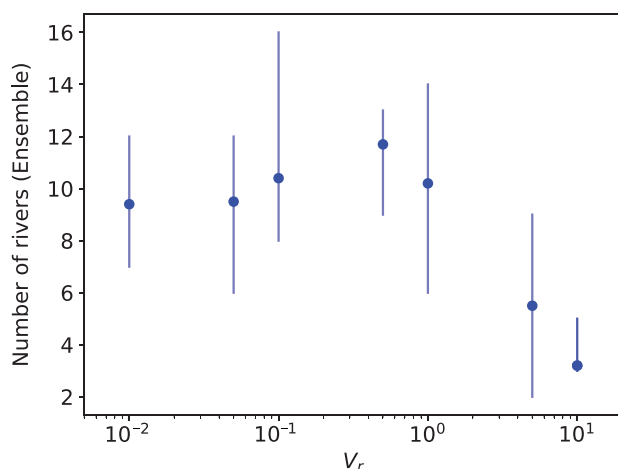


**FIGURE 5** Number of atmospheric rivers as a function of the rainfall parameter,  $V_r$  for  $Q_y = -1$ . Vertical lines are the span of the AR counts for the individual simulations; circles indicates the average number of rivers in each simulation group [Colour figure can be viewed at [wileyonlinelibrary.com](http://wileyonlinelibrary.com)]

horizontal advection (Edwards *et al.*, 2019). This results in  $q_t$  being less filamentary, and therefore in fewer ARs. On the other hand, it is also known that for small  $V_r$  ( $\mathcal{O}(0.1)$ ),  $q_t$  will appear to be very filamentary and lack some of the large-scale structures (Edwards *et al.*, 2019 give illustrations). As one quantitative measure of whether  $q_t$  is filamentary or coherent, Edwards *et al.* (2019) analyzed the spectrum of  $q_t$  variance in Fourier space. The  $q_t$  spectrum can serve as an indicator of the degree of filamentation, as well as an indicator of how the filamentation changes for different  $V_r$  values. The behaviour of the spectrum and filamentation can also be described using a theoretical analysis and scale analysis (Edwards *et al.*, 2019), as summarized here in the present paragraph. For the small  $V_r$  case,  $q_t$  is essentially a passive tracer, as can be seen from Equation (5b), and precipitation will be absent as a driver of AR formation.

In brief, to summarize,  $V_r = \mathcal{O}(1)$  leads to the most realistic or coherent ARs in PQG. If, instead,  $V_r$  is small, then there is not enough precipitation to drive the formation of a coherent AR. At the other extreme, if  $V_r$  is large, then the effects of precipitation will dominate over other processes. In the middle, if  $V_r = \mathcal{O}(1)$ , then the precipitation works in concert with the baroclinic eddies to generate coherent ARs. Referring to the moisture budget in Equation (5a), the ARs involve the influence of precipitation,  $-(V_r/\Delta z)q_t$ , advection,  $D_m q_t/Dt$ , and uplift,  $G_M(L_{ds}/L)w$ .

## 5 | MERIDIONAL WATER TRANSPORT

In this section, we explore the characteristics of meridional water transport. In particular, we focus on the effects of

two parameters – the meridional background gradient of water  $Q_y$ , and the influence of precipitation  $V_r$ . In addition, we also investigate how much of the meridional transport is related to ARs. The moist parameters are fixed with  $V_r = 1$ ,  $Q_y = -1$  unless otherwise noted.

It has been reported that atmospheric rivers in nature can provide more than 90% of the total midlatitude vertically integrated water vapour flux (Zhu and Newell, 1998; Gimeno *et al.*, 2014). To make such an assessment, Zhu and Newell (1998) split the total water flux  $Q_t$  into a “broad flux”  $Q_b$  and a “river flux”  $Q_r$ .

This splitting is computed by

$$Q_r \geq Q_{\text{mean}} + 0.3(Q_{\text{max}} - Q_{\text{mean}}), \quad (7)$$

where  $Q_r$  is the magnitude of the water flux at a given point,  $Q_{\text{mean}}$  is the zonally averaged magnitude of the water flux at the latitude corresponding to the given point, and  $Q_{\text{max}}$  is the maximum magnitude of the water flux at the same latitude. If the inequality holds, the point is considered to be part of the river flux. An example is shown in Figure 6 to illustrate the splitting into river flux and broad flux. This is the example case that was also discussed earlier in Figures 2 and 4. From Figure 6, one can see the intuitive meaning of the splitting: the river flux is defined as the flux that is significantly larger than the zonally averaged flux at a given latitude.

Applying the above criteria to PQG simulations, one might ask how much of the meridional water flux is related to ARs. By taking the zonal average of the plot in Figure 6, it can be seen from Figure 7 that the river flux contains much of the meridional flux, as was seen in observational data (Zhu and Newell, 1998). Generally speaking, Figure 7 shows that the regions between the north and south edges of the zonal jet (roughly  $y \approx 1.5$  and  $y \approx -1.5$ ) contain the strongest zonally averaged meridional flux. For instance, near the south side of the jet at approximately  $y = -1$  (snapshot of  $u_m$  in Figure 2 for reference), the total flux is 0.30 and the river flux is 0.25, so that the river flux accounts for approximately 83% of the total flux. Similarly, near the north side of the jet at approximately  $y = 1.5$ , the total flux is 0.17 and the river flux is 0.10, so that the river flux accounts for approximately 59% of the total flux.

Given that the water flux is strongest at particular latitudes, we next explore connections with the latitudes of largest anomalies of water,  $q_t$ . To see the time evolution, we plot the zonal averages, expressed as  $(\cdot)$ , of  $u_m$ ,  $\theta_e$ ,  $q_t$ ,  $vq_t$ , in Figure 8. To indicate the most important latitudes, the zonal jet can be seen in Figure 8a, which shows zonally averaged  $u_m$ . The zonally averaged potential temperature appears to also have the jet-like structure, with a phase shift in the  $y$ -direction, so that the meridional  $\theta_e$  gradient is strongest at the latitude of the zonal jet. For the water,  $q_t$ ,

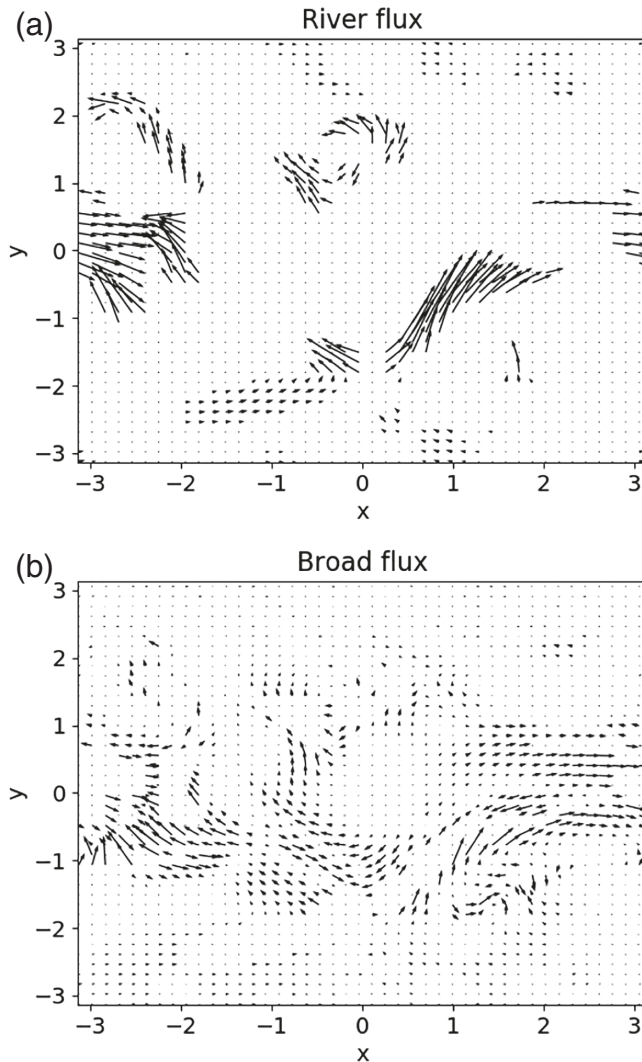


**FIGURE 6** The (a) “river flux” and (b) “broad flux” determined from Equation (7), based on the algorithm of Zhu and Newell (1998)

there is strong positive/negative  $q_t$  above/below the region in the eastward jet with the strongest wind, indicated by the dark-thick (black) line. Figure 8d shows that the meridional transport of water is strongest where the eastward jet is located. Hence, the water  $q_t$  has its maximum to the north of the jet, whereas  $\theta_e$  has its maximum to the south of the jet; and the water flux is aligned with the location of the jet, in a way that contributes to maintaining excess water to the north of the jet.

Another point of interest may be how the meridional water flux behaves over time. To more clearly see the time evolution, Figure 9a,b show the total meridional  $\theta_e$  flux  $\langle v\theta_e \rangle$  and total meridional water flux  $\langle vq_t \rangle$ , respectively, as functions of time, for a long-time simulation (final  $t = 2,000$  compared to the typical value of  $t = 400$ ) with  $V_r = 1$ ,  $Q_y = -1$ . The two curves in each plot indicate

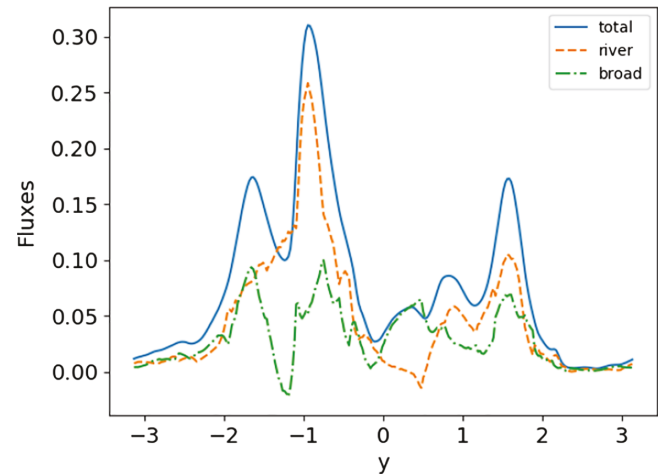


**FIGURE 7** Zonally averaged meridional fluxes where “rivers” are identified by Equation (7), based on the algorithm of Zhu and Newell (1998) [Colour figure can be viewed at [wileyonlinelibrary.com](http://wileyonlinelibrary.com)]

the total flux and the positive flux, which are related by

$$\langle vq_t \rangle_{\text{total}} = \langle vq_t \rangle_{\text{positive}} - |\langle vq_t \rangle_{\text{negative}}|,$$

such that smaller distances between the two curves indicate less negative flux. One noteworthy point is that the flux time series are both intermittent, with maximum flux occurring in bursts at certain times. Comparing Figures 9a and b, one can also see that spikes in  $\langle vq_t \rangle_{\text{total}}$  correspond to spikes in  $\langle v\theta_e \rangle_{\text{total}}$  (for example, compare the peaks at  $t \approx 1,350$ ). Hence, bursts of heat flux and moisture flux seem to occur concomitantly.

Referring to Figure 9, we note again that  $\langle vq_t \rangle_{\text{total}}$  total is always positive, and that there is very little negative flux, since the curves for  $\langle vq_t \rangle_{\text{total}}$  and  $\langle vq_t \rangle_{\text{positive}}$  almost overlap each other. Next, we show how the positive and negative contributions to the total meridional flux  $\langle vq_t \rangle_{\text{total}}$  are affected by changes in the parameters moist  $Q_y$  and  $V_r$ .

To contrast the cases  $Q_y = -1$  and  $Q_y = 0$  while keeping  $V_r = 1$  fixed, the case with  $Q_y = -1$  is re-plotted in Figure 10, for ease of comparison to the case with  $Q_y = 0$  shown in Figure 11. For  $Q_y = -1$ , as discussed above, Figure 10 shows that the total meridional flux is mostly positive.

For  $Q_y = 0$ , Figure 11 shows that the total meridional flux is centred around zero, and indicates that the negative flux is significant. Therefore, as one might expect, the meridional gradient  $Q_y$  allows for the meridional water flux to be non-zero and positive in our simulations.

Finally, we illustrate how meridional water flux changes as the rainfall parameter  $V_r$  varies, while keeping

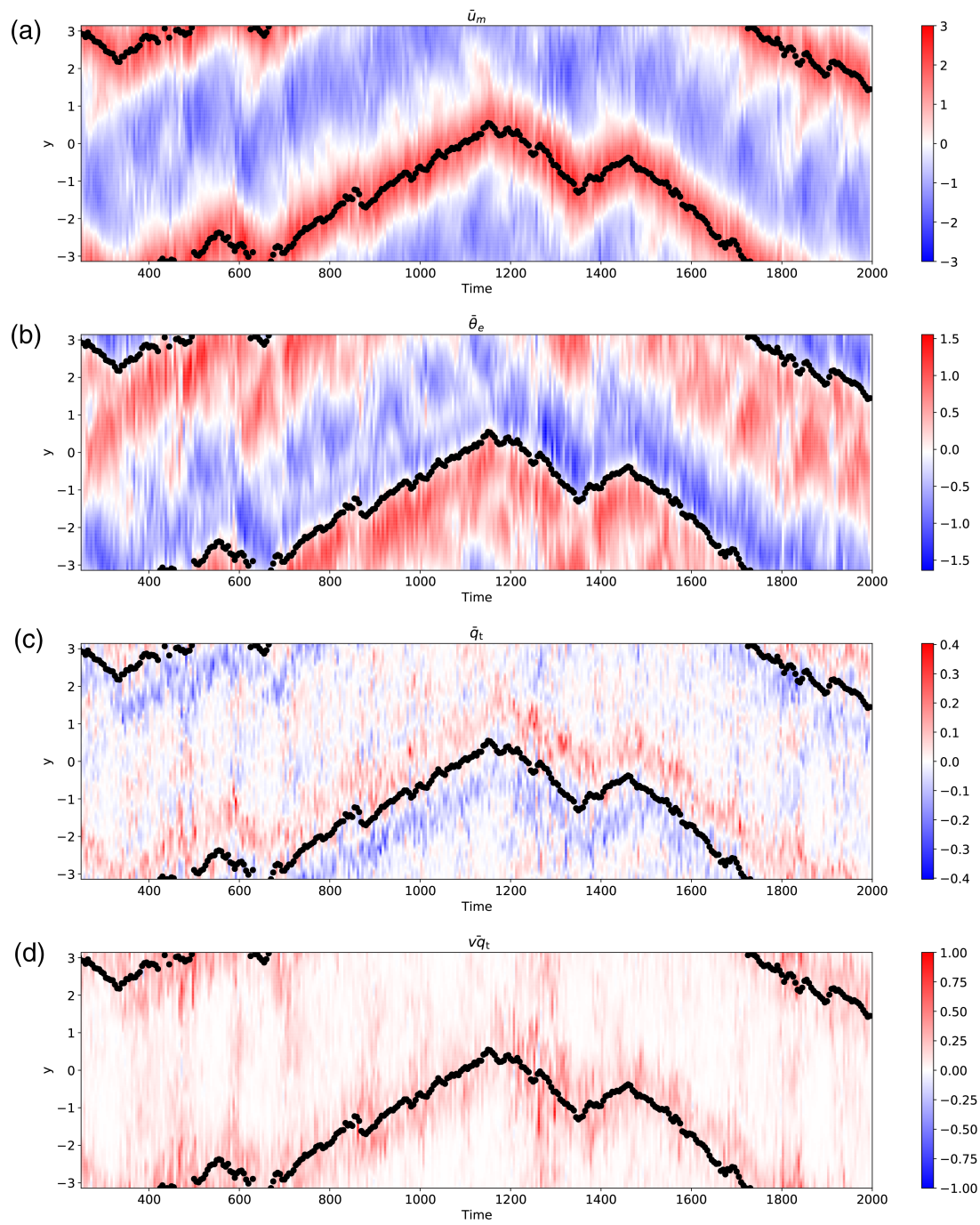


**FIGURE 8** Zonally averaged (a)  $u_m$ , (b)  $\theta_e$ , (c)  $q_t$ , (d)  $vq_t$  as a function of time, with  $V_r = 1$  and  $Q_y = -1$ . The dark-thick (black) line represents the location where zonally averaged  $u_m$  is the strongest [Colour figure can be viewed at [wileyonlinelibrary.com](http://wileyonlinelibrary.com)]

the background flux  $Q_y = -1$  held fixed. Comparing Figures 10 ( $V_r = 1$ ) and 12 ( $V_r = 0.1$  and  $V_r = 10$ ), one can see that the amplitude of the total flux decreases with increasing  $V_r$ , as expected from the dissipative nature of the rainfall term. An interesting feature, however, is that with increasing  $V_r$ , the positive flux converges to the total flux, indicating that there is less negative flux. Once  $V_r$  is strong enough, the total flux appears to be almost always positive. This fact can also be seen by computing the

average ratio of the total flux to the positive flux, as shown in Table 5.

## 6 | ADDITIONAL PARAMETER STUDIES

In addition to the parameters  $V_r$  and  $Q_y$  which were varied above (e.g., 70 total simulations were conducted to explore

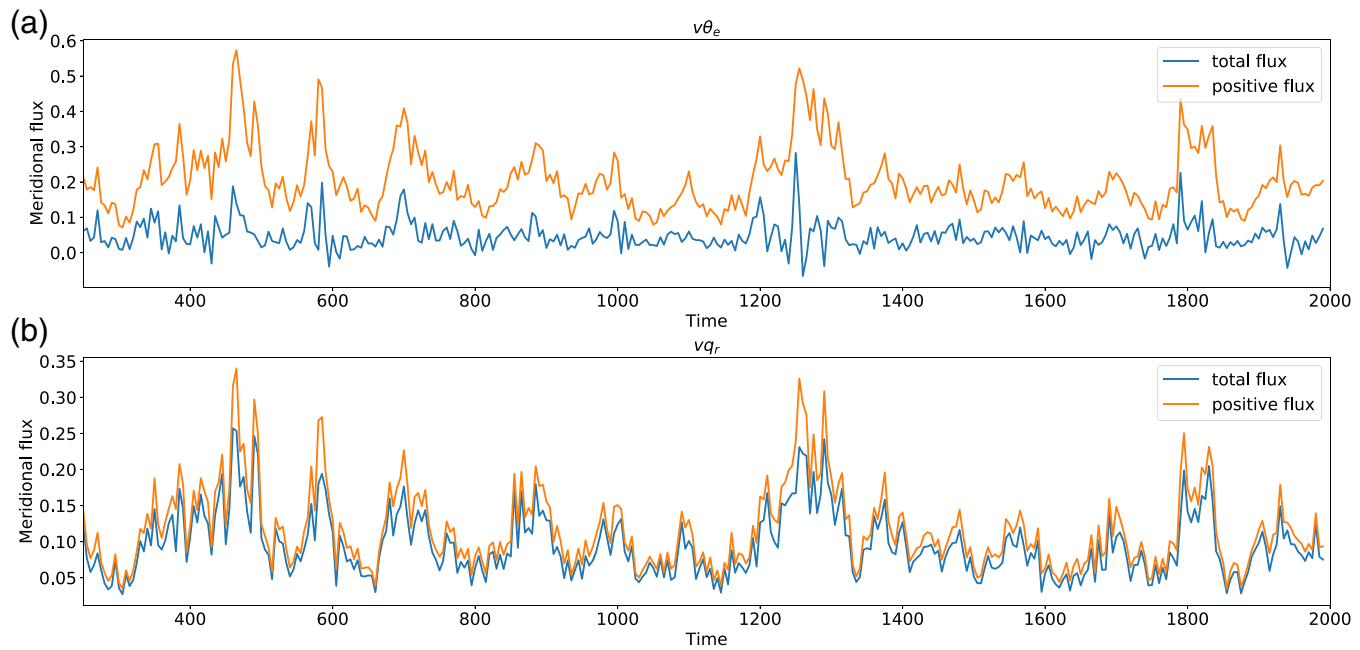


**FIGURE 9** (a) The total meridional  $\theta_e$  flux  $\langle v\theta_e \rangle$  and (b) the total meridional water flux  $\langle vq_t \rangle$  as a function of time, with  $V_r = 1$  and  $Q_y = -1$  [Colour figure can be viewed at [wileyonlinelibrary.com](http://wileyonlinelibrary.com)]

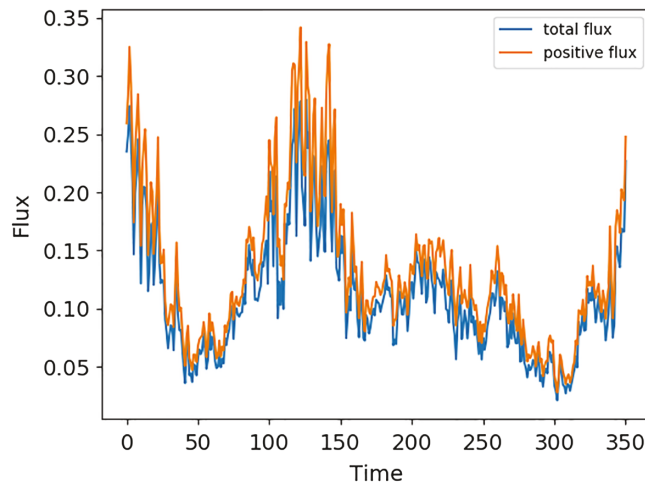


**FIGURE 10** The total meridional flux  $\langle vq_t \rangle$  as a function of time, with  $V_r = 1$  and  $Q_y = -1$  [Colour figure can be viewed at [wileyonlinelibrary.com](http://wileyonlinelibrary.com)]

seven different  $V_r$  values), the dry parameters such as  $\beta$ , and the other moist parameter  $G_M$ , can potentially affect some of the behaviour of the water flux and presence of ARs.

Based on some preliminary simulations done with different values of  $\beta$ , it was observed that when the jet was stronger, water would organize near the jet boundary more consistently, whereas for the case of a weak jet which would intermittently show vortical behaviour, the organization of water seemed to be less coherent. However, for both  $\beta = 2$  and  $\beta = 3$ , the numbers of ARs identified were

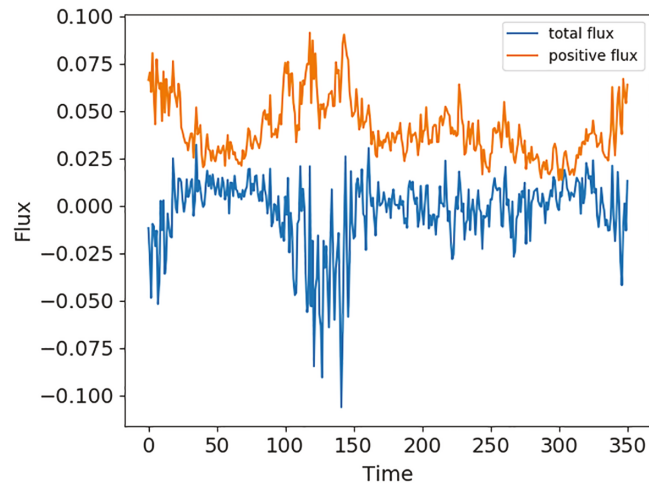


**FIGURE 11** The total meridional flux  $\langle vq_t \rangle$  as a function of time, with  $V_r = 1$  and  $Q_y = 0$ . The total meridional flux seems to be centred around zero [Colour figure can be viewed at [wileyonlinelibrary.com](http://wileyonlinelibrary.com)]

23 and 15, and are comparable in order of magnitude to the  $\beta = 2.5$  case used in the other sections where the number of ARs observed ranged from 6 to 14. The less coherent nature of the zonal jet for  $\beta = 2$  contributed to the higher counts in the ARs.

Simulations with different values of  $G_M$  were also compared. For values of  $G_M = 1.1$  and  $G_M = 1.5$ , there appeared to be no significant differences from the case  $G_M = 1$ , except for slight differences in amplitude, as can be seen in Figure 13. A 10% change in  $G_M$  appears to

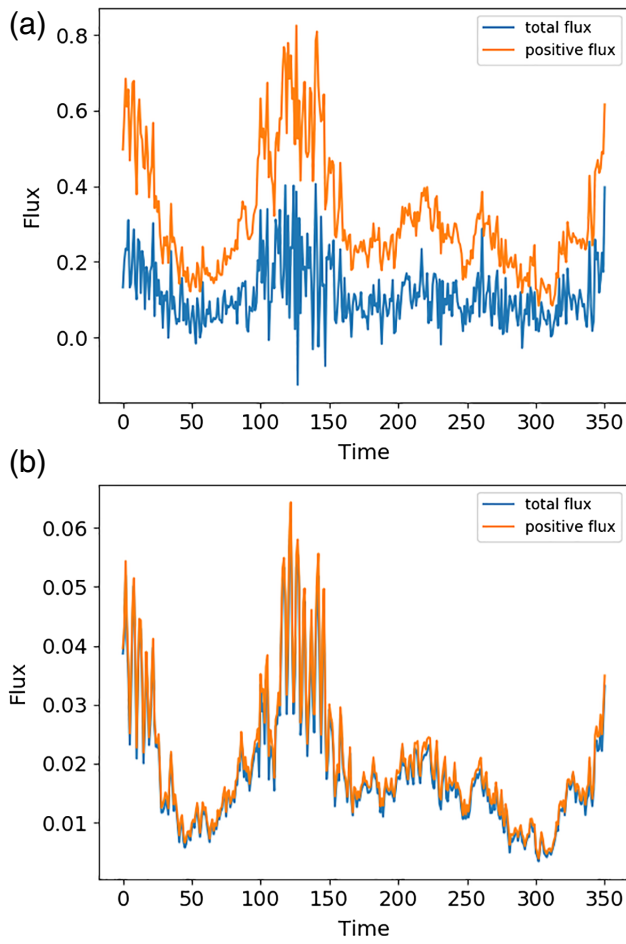


**FIGURE 12** The total meridional flux  $\langle vq_t \rangle$  as a function of time for (a)  $V_r = 0.1$  and (b)  $V_r = 10$ , both with  $Q_y = -1$  [Colour figure can be viewed at [wileyonlinelibrary.com](http://wileyonlinelibrary.com)]

**TABLE 5** The ratio between the total meridional water flux and the positive meridional water flux averaged over time

$V_r$	$\langle vq_t \rangle_{\text{total}} / \langle vq_t \rangle_{\text{positive}}$
0.01	0.161
0.1	0.654
1	0.838
10	0.929

Note: Larger values of  $V_r$  mean that the amount of negative flux decreases and the total flux is composed mostly of the positive flux.

change the amplitude by approximately 10%, and the number of ARs identified were 14 for both cases  $G_M = 1$  and 1.1. In this model, it is known that changing  $G_M$  will result in the large scales having more differences than the smaller scales (Edwards *et al.*, 2019). This can also be seen from the “Difference” plot from Figure 13, where the main difference is in the large scales.

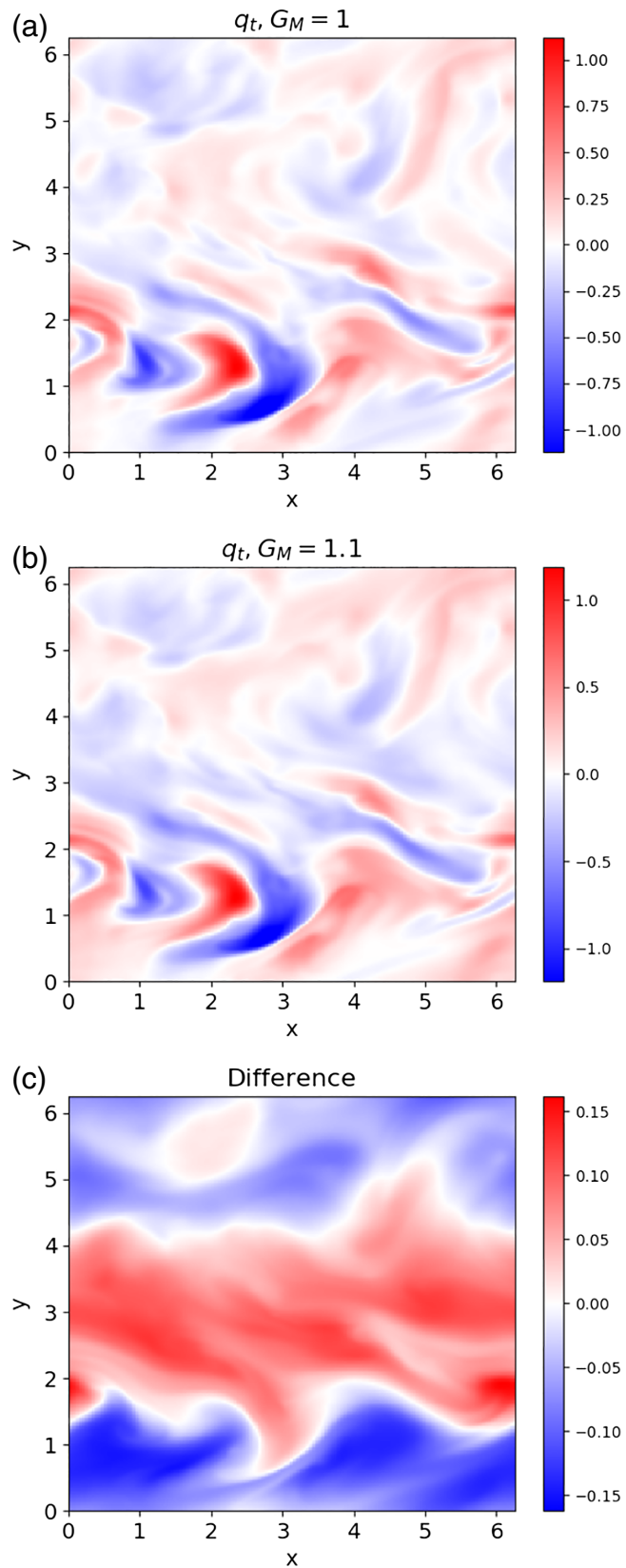


**FIGURE 13** Snapshots of  $q_t$  with (a)  $G_M = 1$ , (b)  $G_M = 1.1$  and (c) the difference between the two, all with  $V_r = 1$  and  $Q_y = -1$  [Colour figure can be viewed at [wileyonlinelibrary.com](http://wileyonlinelibrary.com)]

## 7 | CONCLUSIONS

In summary, our objective was to investigate the presence of ARs in a moist QG framework. The two-level PQG equations were used in a saturated, precipitating environment without phase changes, in order to explore cases with reduced complexity. The idea is the following: if this case can produce idealized ARs, then one would expect that further realism can be achieved by incorporating more physics, such as phase changes and additional vertical levels.

Even within our simple model set-up, the simulations demonstrate that ARs are identified by a commonly used AR identification algorithm (Guan and Waliser, 2015). Moreover, as in nature, it was seen that the model ARs contribute a substantial amount of meridional moisture flux relative to their small and narrow size.

To produce the model ARs, two main moist ingredients were needed, beyond the baroclinic instability that is typical of QG frameworks: precipitation and a meridional moisture gradient. Associated with these ingredients are two parameters –  $V_r$  and  $Q_y$ , respectively – and if either ingredient is too weak, then the model ARs are less frequent and contribute less significantly to the meridional water transport. The QG framework includes some of the rudimentary physical mechanisms seen in the water vapour budgets of ARs in nature (e.g., Cordeira *et al.*, 2013; Hecht and Cordeira, 2017), including horizontal convergence of water vapour associated with ascent, along with precipitation.

Overall, this study suggests that the PQG model can help to elucidate large-scale features of the midlatitude atmosphere that are intimately connected to the presence of water. In the future, the full version of PQG with phase changes (Smith and Stechmann, 2017) could allow for further insight. It would also be interesting to investigate and compare ARs in a hierarchy of models of varying complexity. For instance, global climate model studies allow a more comprehensive treatment including land effects (e.g., Payne and Magnusdottir, 2015; Warner *et al.*, 2015), and aquaplanet studies without land could offer another level of intermediate complexity within a model hierarchy (e.g., Hagos *et al.*, 2015).

## ACKNOWLEDGEMENTS

The authors thank two anonymous reviewers for helpful comments. This research was partially supported by grants from the National Science Foundation Division of Atmospheric and Geospace Sciences (no. 1443325), Division of Mathematical Sciences (no. 1147523), and the University of Wisconsin-Madison Office of the Vice Chancellor for Research and Graduate Education with funding from the Wisconsin Alumni Research Foundation.

## ORCID

Thomas K. Edwards  <https://orcid.org/0000-0003-0069-9424>

## REFERENCES

Bannon, P.R. (1986) Linear development of quasi-geostrophic baroclinic disturbances with condensational heating. *Journal of the Atmospheric Sciences*, 43(20), 2261–2274.

Charney, J.G. (1947) The dynamics of long waves in a baroclinic westerly current. *Journal of Meteorology*, 4(5), 136–162.

Charney, J.G. (1948) On the scale of atmospheric motions. *Geofysiske Publikasjoner Oslo*, 17(2), 1–17.

Cordeira, J.M., Ralph, F.M. and Moore, B.J. (2013) The development and evolution of two atmospheric rivers in proximity to western North Pacific tropical cyclones in October 2010. *Monthly Weather Review*, 141(12), 4234–4255.

Dacre, H.F., Clark, P.A., Martinez-Alvarado, O., Stringer, M.A. and Lavers, D.A. (2015) How do atmospheric rivers form?. *Bulletin of the American Meteorological Society*, 96(8), 1243–1255.

Dettinger, M. (2011) Climate change, atmospheric rivers, and floods in California – a multimodel analysis of storm frequency and magnitude changes 1. *Journal of the American Water Resources Association*, 47(3), 514–523.

Edwards, T.K., Smith, L.M. and Stechmann, S.N. (2019) Spectra of atmospheric water in precipitating quasi-geostrophic turbulence. *Geophysical & Astrophysical Fluid Dynamics*. <https://doi.org/10.1080/03091929.2019.1692205>

Gao, Y., Lu, J., Leung, L.R., Yang, Q., Hagos, S. and Qian, Y. (2015) Dynamical and thermodynamical modulations on future changes of landfalling atmospheric rivers over western North America. *Geophysical Research Letters*, 42(17), 7179–7186.

Gimeno, L., Dominguez, F., Nieto, R., Trigo, R., Drumond, A., Reason, C.J., Taschetto, A.S., Ramos, A.M., Kumar, R. and Marengo, J. (2016) Major mechanisms of atmospheric moisture transport and their role in extreme precipitation events. *Annual Review of Environment and Resources*, 41, 117–141.

Gimeno, L., Nieto, R., Vázquez, M. and Lavers, D.A. (2014) Atmospheric rivers: a mini-review. *Frontiers in Earth Science*, 2. <https://doi.org/10.3389/feart.2014.00002>.

Guan, B. and Waliser, D.E. (2015) Detection of atmospheric rivers: evaluation and application of an algorithm for global studies. *Journal of Geophysical Research: Atmospheres*, 120(24), 12514–12535.

Hagos, S., Leung, L.R., Yang, Q., Zhao, C. and Lu, J. (2015) Resolution and dynamical core dependence of atmospheric river frequency in global model simulations. *Journal of Climate*, 28(7), 2764–2776.

Hecht, C.W. and Cordeira, J.M. (2017) Characterizing the influence of atmospheric river orientation and intensity on precipitation distributions over North Coastal California. *Geophysical Research Letters*, 44(17), 9048–9058.

Held, I.M. and O'Brien, E. (1992) Quasigeostrophic turbulence in a three-layer model: effects of vertical structure in the mean shear. *Journal of the Atmospheric Sciences*, 49(19), 1861–1870.

Hernandez-Duenas, G., Majda, A.J., Smith, L.M. and Stechmann, S.N. (2013) Minimal models for precipitating turbulent convection. *Journal of Fluid Mechanics*, 717, 576–611.

Jiang, T., Evans, K.J., Deng, Y. and Dong, X. (2014) Intermediate frequency atmospheric disturbances: a dynamical bridge connecting western U.S. extreme precipitation with East Asian cold surges. *Journal of Geophysical Research: Atmospheres*, 119(7), 3723–3735.

Kessler, E. (1969) *On the distribution and continuity of water substance in atmospheric circulations*. Meteorological Monographs No. 32, American Meteorological Society, Boston, MA.

Lamberts, J., Lapeyre, G. and Zeitlin, V. (2012) Moist versus dry baroclinic instability in a simplified two-layer atmospheric model with condensation and latent heat release. *Journal of the Atmospheric Sciences*, 69(4), 1405–1426.

Lapeyre, G. and Held, I. (2004) The role of moisture in the dynamics and energetics of turbulent baroclinic eddies. *Journal of the Atmospheric Sciences*, 61(14), 1693–1710.

Lavers, D.A., Allan, R.P., Wood, E.F., Villarini, G., Brayshaw, D.J. and Wade, A.J. (2011) Winter floods in Britain are connected to atmospheric rivers. *Geophysical Research Letters*, 38(23). <https://doi.org/10.1029/2011GL049783>.

Lavers, D.A., Villarini, G., Allan, R.P., Wood, E.F. and Wade, A.J. (2012) The detection of atmospheric rivers in atmospheric reanalyses and their links to British winter floods and the large-scale climatic circulation. *Journal of Geophysical Research: Atmospheres*, 117(D20). <https://doi.org/10.1029/2012JD018027>.

Mak, M. (1982) On moist quasi-geostrophic baroclinic instability. *Journal of the Atmospheric Sciences*, 39(9), 2028–2037.

Monteiro, J.M. and Sukhatme, J. (2016) Quasi-geostrophic dynamics in the presence of moisture gradients. *Quarterly Journal of the Royal Meteorological Society*, 142, 187–195.

Nayak, M.A., Villarini, G. and Lavers, D.A. (2014) On the skill of numerical weather prediction models to forecast atmospheric rivers over the central United States. *Geophysical Research Letters*, 41(12), 4354–4362.

Neiman, P.J., Ralph, F.M., Wick, G.A., Lundquist, J.D. and Dettinger, M.D. (2008) Meteorological characteristics and overland precipitation impacts of atmospheric rivers affecting the west coast of North America based on eight years of SSM/I satellite observations. *Journal of Hydrometeorology*, 9(1), 22–47.

Neiman, P.J., White, A.B., Ralph, F.M., Gottas, D.J. and Gutman, S.I. (2009) A water vapour flux tool for precipitation forecasting. (Vol. 162), pages 83–94.

Payne, A.E. and Magnusdottir, G. (2015) An evaluation of atmospheric rivers over the North Pacific in CMIP5 and their response to warming under RCP 8.5. *Journal of Geophysical Research: Atmospheres*, 120(21), 11–173.

Pedlosky, J. (2013) *Geophysical Fluid Dynamics*. Springer, Berlin.

Phillips, N.A. (1954) Energy transformations and meridional circulations associated with simple baroclinic waves in a two-level, quasi-geostrophic model. *Tellus*, 6(3), 274–286.

Qi, D. and Majda, A.J. (2016) Low-dimensional reduced-order models for statistical response and uncertainty quantification: two-layer baroclinic turbulence. *Journal of the Atmospheric Sciences*, 73(12), 4609–4639.

Ralph, F.M., Neiman, P.J. and Wick, G.A. (2004) Satellite and CAL-JET aircraft observations of atmospheric rivers over the eastern North Pacific Ocean during the winter of 1997/98. *Monthly Weather Review*, 132(7), 1721–1745.

Ralph, F.M. and Dettinger, M. (2011) Storms, floods, and the science of atmospheric rivers. *Eos*, 92(32), 265–266.

Ralph, F.M., Coleman, T., Neiman, P., Zamora, R. and Dettinger, M. (2013) Observed impacts of duration and seasonality of atmospheric-river landfalls on soil moisture and runoff in coastal northern California. *Journal of Hydrometeorology*, 14(2), 443–459.

Ralph, F.M., Dettinger, M.D., Cairns, M.M., Galarneau, T.J. and Eylander, J. (2018) Defining “atmospheric river”: how the Glossary of Meteorology helped resolve a debate. *Bulletin of the American Meteorological Society*, 99(4), 837–839.

Ralph, F.M., Rutz, J.J., Cordeira, J.M., Dettinger, M., Anderson, M., Reynolds, D., Schick, L.J. and Smallcomb, C. (2019) A scale to characterize the strength and impacts of atmospheric rivers. *Bulletin of the American Meteorological Society*, 100, 269–289.

Rhines, P.B. (1979) Geostrophic turbulence. *Annual Review of Fluid Mechanics*, 11(1), 401–441.

Rutz, J.J., Steenburgh, W.J. and Ralph, F.M. (2014) Climatological characteristics of atmospheric rivers and their inland penetration over the western United States. *Monthly Weather Review*, 142(2), 905–921.

Salmon, R. (1980) Baroclinic instability and geostrophic turbulence. *Geophysical & Astrophysical Fluid Dynamics*, 15(1), 167–211.

Salmon, R. (1998) *Lectures on Geophysical Fluid Dynamics*. Oxford University Press, Oxford, UK.

Smith, B.L., Yuter, S.E., Neiman, P.J. and Kingsmill, D. (2010) Water vapor fluxes and orographic precipitation over Northern California associated with a landfalling atmospheric river. *Monthly Weather Review*, 138(1), 74–100.

Smith, L.M. and Stechmann, S.N. (2017) Precipitating quasi-geostrophic equations and potential vorticity inversion with phase changes. *Journal of the Atmospheric Sciences*, 74, 3285–3303.

Vallis, G.K. (2006) *Atmospheric and oceanic fluid dynamics*. Cambridge University Press, Cambridge, UK.

Waliser, D.E., Moncrieff, M.W., Burridge, D., Fink, A.H., Gochis, D., Goswami, B., Guan, B., Harr, P., Heming, J., Hsu, H.-H., Jakob, C., Janiga, M., Johnson, R., Jones, S., Knippertz, P., Marengo, J., Nguyen, H., Pope, M., Serra, Y., Thorncroft, C.D., Wheeler, M., Wood, R. and Yuter, S. (2012) The “year” of tropical convection (May 2008–April 2010): climate variability and weather highlights. *Bulletin of the American Meteorological Society*, 93(8), 1189–1218.

Warner, M.D., Mass, C.F. and Salathé Jr, E.P. (2015) Changes in winter atmospheric rivers along the North American west coast in CMIP5 climate models. *Journal of Hydrometeorology*, 16(1), 118–128.

Wetzel, A.N., Smith, L.M. and Stechmann, S.N. (2017) Moisture transport due to baroclinic waves: linear analysis of precipitating quasi-geostrophic dynamics. *Mathematics of Climate and Weather Forecasting*, 3(1), 28–50. <https://doi.org/10.1515/mcwf-2017-0002>.

Wick, G.A., Neiman, P.J. and Ralph, F.M. (2013) Description and validation of an automated objective technique for identification and characterization of the integrated water vapor signature of atmospheric rivers. *IEEE Transactions on Geoscience and Remote Sensing*, 51(4), 2166–2176.

Zhu, Y. and Newell, R.E. (1998) A proposed algorithm for moisture fluxes from atmospheric rivers. *Monthly Weather Review*, 126(3), 725–735.

**How to cite this article:** Edwards TK, Smith LM, Stechmann SN. Atmospheric rivers and water fluxes in precipitating quasi-geostrophic turbulence. *Q.J.R. Meteorol. Soc.* 2020;146:1960–1975. <https://doi.org/10.1002/qj.3777>